Engineering Science and Technology, an International Journal 21 (2018) 639–653

HOSTED BY

Contents lists available at ScienceDirect

Engineering Science and Technology, an International Journal

journal homepage: www.elsevier.com/locate/jestch

Full Length Article

A new topology with the repetitive controller of a reduced switch seven-level cascaded inverter for a solar PV-battery based microgrid

Buddhadeva Sahoo, Sangram Keshari Routray *, Pravat Kumar Rout

SOA University, India

ARTICLE INFO

Article history:
Received 17 January 2018
Revised 22 May 2018
Accepted 5 June 2018
Available online 15 June 2018

Keywords:
Battery cell
Photovoltaic cell
MPPT technique
Reduced switch cascaded inverter (RSCI)
LCL filters
Repetitive control (RC)
Incremental conductance (IC)

ABSTRACT

In this manuscript, a repetitive control approach for the reduced switch seven-level cascaded inverter (RSCI) is proposed for active and reactive power control with enhanced power quality standard for a solar PV-battery based microgrid. The proposed repetitive control approach is applied for the RSCI and the performance is tested on a grid-connected microgrid integrated with photovoltaic (PV) and battery energy sources. To capture maximum power, a control strategy based on incremental conductance method (I&C) is adapted for optimal maximum power point tracking (MPPT) operation. The battery energy storage system in both charging and discharging mode of operation is controlled by repetitive controlled based RSCI as a support to PV for better power management. To show the feasibility and robustness in operation of the proposed approach, a variable irradiance input to the PV unit is considered. To justify the practical applicability of the proposed approach and to satisfy IEEE-1547 power quality constraints, a LCL filter is selected to minimize the harmonic distortion in the grid side current levels. The improved performance of the proposed technique is justified by presenting comparative simulation results with respect to three-level neutral point clamped inverter (NPC) with proportional integral (PI) controller. By using MATLAB software, the validity of the proposed approach is studied by simulation under constant and varying irradiance condition.

1. Introduction

In the energy generation sector, due to the pollution and energy crisis in the world, distributed generation has been merged as a solution with advanced semiconductor based power electronic devices and smart grid technology [1–3]. Even though the distribution generation (DG) system plays an important role in the power system, it has also come with the challenges to look forward and find out an optimal solution for control and protection [4–6]. PV system gives more attractive features for which it is widely accepted and widely implemented in various power sectors of different countries. Specific to a distribution system, PV is chosen in renewable energy sectors because it permits small power generators for installation purpose and gives low or medium voltage levels [7,14].

In real-time applications of PV-battery based microgrid, single-stage and two-stage inverters are used by voltage source based advanced power electronic devices for power conversion system. In two-stage conversion system, one converter is used to change pulsating DC to constant DC and the other converter is used to change constant DC to AC for better power quality and efficiency [15]. To execute the single stage conversion system, a multilevel inverter is preferable to implement instead of conventional voltage source inverter (VSI), as it gives more voltage levels with minimize voltage error and harmonics [16]. In renewable energy sectors to enhance the power generation capability and reliability of power management under varying environmental depended input, the MPPT control is needed to implement. There are many methods are suitable for uniform and varying irradiance condition [17,18]. The incremental conductance method is widely used for inverter control to generate maximum power to the grid or to the load. The attractive feature behind its preference is improved results in most condition and easy to implement in a digital controller.

Various multi-level inverter (MLI) topologies are suggested by the various researcher based on three-level Neutral point clamped inverter (NPC), Flying capacitor inverter (FCI) and Cascaded inverter (CI) [20,26]. However, the major limitation to be focused on a better solution of these types of inverters is the requirement of a large number of power electronic switches, capacitors, and diodes. Furthermore, with the increase in the voltage levels, the number of

* Corresponding author.
E-mail address: routraysk@gmail.com (S.K. Routray).
Peer review under responsibility of Karabuk University.

https://doi.org/10.1016/j.jestch.2018.06.007
2215-0986/

components is also increased. It is necessary to focus on the configuration and the control aspects of the integrated converter during the design stage to find solutions for simple design, cost effectiveness, better power control and power quality issues.

The PI controllers are widely used in real-time applications due to its simple design structure and cost-effectiveness. However, these controller performances depend on their gain parameters. Due to use of constant gain parameters, these controllers fail to show their optimum performance with a change in the system and input variations under different operating conditions. To enhance the controller performance and to overcome the associated limitations of PI controllers various suggestions are proposed by various authors such as fuzzy tuned PI controller, adaptive PI controller, self tuned PI controller and evolutionary optimized PI controller etc. [27–29]. Other possibility is to use different control strategy for the controller. In addition to power control, it is also necessary for the inverter control to eliminate the THD. In this aspect the repetitive control (RC) can track or eliminate periodic signals in an effective way, particularly in case of closed loop system application. RC based controller is effective to track or eliminate any periodic signals including any order harmonics due to its superior error cancelation characteristics [30–36]. RC controller application has been extensively investigated for multi-level inverter in this study. The LCL filter is used to further reduce harmonic distortion at the inverter side (AC) voltage and current, and also to act as a protection for its capability to suppress any sudden change in voltage due to harmonics [37,38].

One of the major concerns of PV-battery based microgrid systems is their unpredictable, non-linear and fluctuating nature. Due to extensive use of power electronic devices, power quality issues degrade the operational performance of the system. The urgent requirements of high power consuming industrial sectors need a medium to high voltage distribution system with better power management, voltage and frequency control. Grid connected renewable energy systems accompanied by battery energy storage, appropriate filter, and proper inverter control to overcome all these above mentioned issues. This paper is concerned with the designed and study of a grid connected three phase solar PV system integrated with battery storage, LCL filter, and reduced switch seven-level cascaded inverter (RSCI). The feasibility of the proposed system is obtained under fixed and varying irradiance condition. The proposed control approach based on repetitive control and incremental conductance (IC) has the capability of regulating MPPT, harmonic elimination, better power control, and battery charging and discharging conditions. The proposed approach is verified and results indicate a better power flow control with enhanced power quality, increased efficiency, and reliability. The major contributions of this paper inline to its objectives are as follows:

- To design a repetitive controller for power control regulation.
- To design a RSCI for energy storage based PV microgrid.
- To integrate MPPT technique with different irradiance condition to extract maximum available energy.
- To ensure the harmonic levels within the IEEE-1547 standard for better power quality improvement.

The rest part of the manuscript is coordinated as follows. Section 2 presents the modeling of the photovoltaic system and reduced switch seven-level cascaded inverter (RSCI). The design of LCL filter is also presented in this section. Control of MPPT, vector selections, d-q current and battery conditions along with repetitive control are described in Section 3. In Section 4 simulation results under various operating conditions are demonstrated and analyzed to justify the applicability of the proposed approach in the real-time application. Section 5 concludes the manuscript mentioning the output analysis and findings of this work.

2. Modeling

The test system comprised of PV-battery based microgrid with grid support RSCI inverter control is considered for verifying the

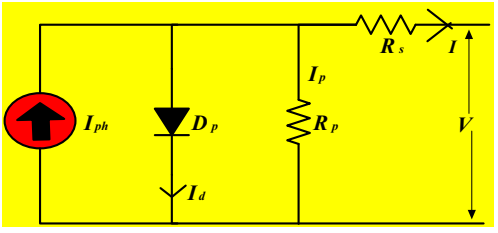

Fig. 2. Equivalent circuit of single diode PV cell.

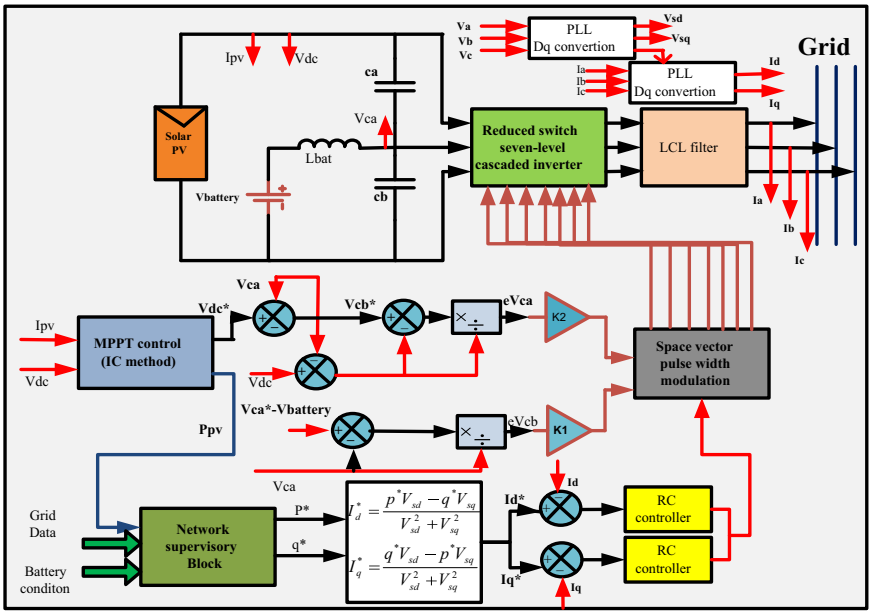

Fig. 1. Block diagram of the control system to integrate PV and battery storage.

proposed approach. Fig. 1 shows the whole system along with the other associated component such as LCL filter, PV battery storage, and the controller in a block diagram form of representation.

2.1. Modeling of photovoltaic system

The equivalent circuit of a single diode model of a PV cell consists of a light generated photo current (I_{ph}), a diode (D_p), parallel resistor (R_p) and a series resistor (R_s) is illustrated in Fig. 2.

For an ideal PV cell, the total current (I) is computed as [3,4]:

$$I = I_{ph} - I_o\left(e^{\left(\frac{qV}{N_s aKT_w}\right)} - 1\right) - \frac{V + IR_s}{R_p} \tag{1}$$

where 'I_d' denotes the diode current of the PV cell and represented as:

$$I_d = I_o\left(e^{\left(\frac{qV}{aKT_w}\right)} - 1\right) \tag{2}$$

where I_o is the cell saturation dark current (A), q is the charge of the electron (C), K is the Boltzmann constant (J/K), T_w is the working temperature of the cell (K), and 'a' is known as the ideality factor (eV) of the system. For fixed temperature and solar irradiation condition, the voltage and current relationship of the PV cell is computed as [5–7]:

The photo current 'I_{ph}' also depends upon the solar irradiance and the working temperature, and can be calculated as:

$$I_{ph} = \frac{G_w}{G_{ref}}(I_{sc} + Ki(T_w - T_{ref})) \tag{3}$$

where N_s is known as number of series connected PV cell, T_{ref} is the reference temperature of the cell (K), Ki is the cell short circuit current temperature coefficient (A/K), I_{sc} is the short circuit current of the cell (A), G_{ref} and G_w are the reference irradiance and working irradiance conditions (W/m^2) respectively. The cell saturation current (I_o) depends upon the cell temperature and represented as [8–10]:

$$I_o = I_{on}\left(\frac{T_w}{T_{ref}}\right)^3 \exp\left(\frac{q}{aK}\left(\frac{E_{g,T_{ref}}}{T_{ref}} - \frac{E_{g,T_w}}{T_w}\right)\right) \tag{4}$$

where I_{on} is the reverse saturation current of the cell at a reference temperature (K) and solar irradiance (W/m^2). E_{g,T_w} is the material band gap (eV) of the PV cell. E_{g,T_w} exhibits small temperature dependence and computed as [8–10]:

$$E_{g,T_w} = E_{g,T_{ref}} \times [1 - 0.0002677(T_w - T_{ref})] \tag{5}$$

where $E_{g,T_{ref}}$ is 1.121 eV for silicon cell.

Due to implicit and non linear nature of the above equations; it is difficult to reach an analytic solution for the PV model parameters at a constant temperature and irradiance. The photocurrent (Iph) is higher than the cell saturation current (Io) and so the small diode and leakage current are neglected under short circuit condi-

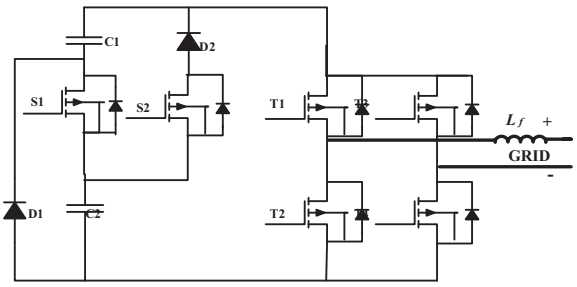

Fig. 5. Circuit diagram of two phase RSCI.

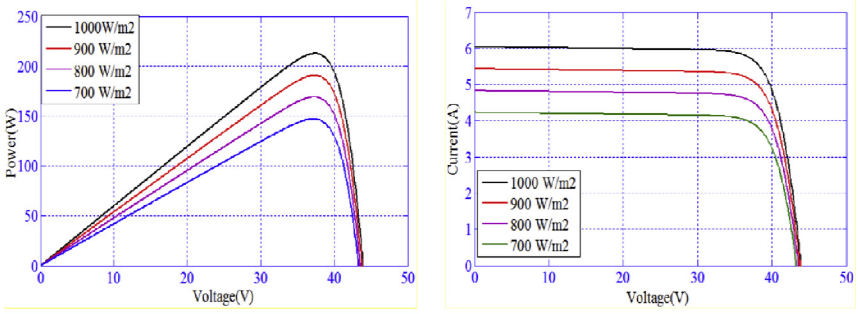

a b

Fig. 3. P-V characteristics curves operated at different irradiance condition conditions. (a) Power (W) vs. Voltage (V) curve (b) Current (A) vs. Voltage (V) curve.

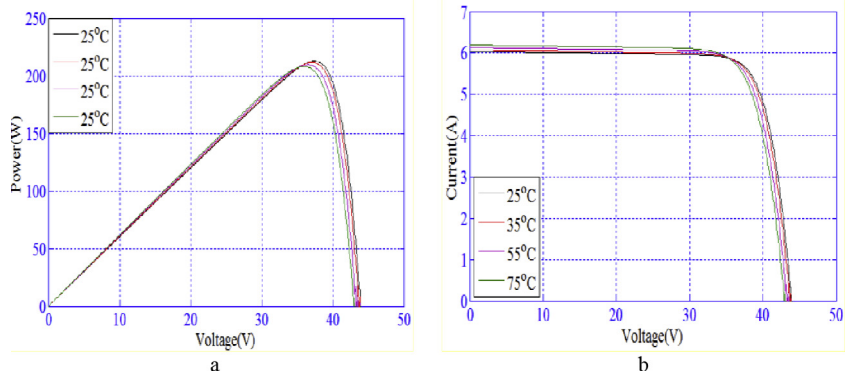

a b

Fig. 4. P-V characteristics curves operated at different temperature conditions. (a) Power (W) vs. Voltage (V) curve (b) Current (A) vs. Voltage (V) curve.

tions. The short circuit current (Isc) is nearly equal to the light generated photo current and represented as:

$$I_{ph} = I_{sc} \tag{6}$$

For open circuit condition, the open circuit voltage (V_{oc}) is calculated by assuming the output current as zero. By neglecting the parallel leakage current (I_p), the reverse saturation current (I_{on}) at a reference temperature can be computed as [11,12]:

$$I_{on} = \frac{I_{sc}}{\exp\left(\frac{qV_{oc}}{N_s aKT_w}\right) - 1} \tag{7}$$

To validate the PV model, its performance characteristics power (W) vs voltage (V_{oc}) and voltage (V_{oc}) vs current (I_{ph}) test results under different irradiance and temperature (T_{act}) conditions are demonstrated in Figs. 3 and 4 respectively [13,14].

2.2. Modeling of a reduced switch seven-level cascaded inverter (RSCI)

RSCI contains a full bridge three-phase inverter and a capacitor selection circuit connected in cascade. The inverter operates in both upper half cycle (+ve) and lower half cycle (−ve). The power electronic switches and diodes are assumed to be ideal, when the voltages across two capacitors are constant and equal to $\frac{V_{dc}}{3}$ and $\frac{2V_{dc}}{3}$ respectively [23,24]. As the output current comes from the generation side (PV) is in phase with grid voltage, the output current of the inverter side (RSCI) are also in phase with the voltage of the grid. The operation of the inverter is broadly divided into 8 modes of operation: 4 modes belong to upper half cycle (+ve) and another 4 modes belong to lower half cycle (−ve). Fig. 5 demonstrated the circuit diagram of the two-phase RSCI [25].

The Operational equivalent circuit diagram of seven-level inverter for upper half cycle of (a) *case 1*, (b) *case 2*, (c) *case 3*, and (d) *case 4* are illustrated in Fig. 6.

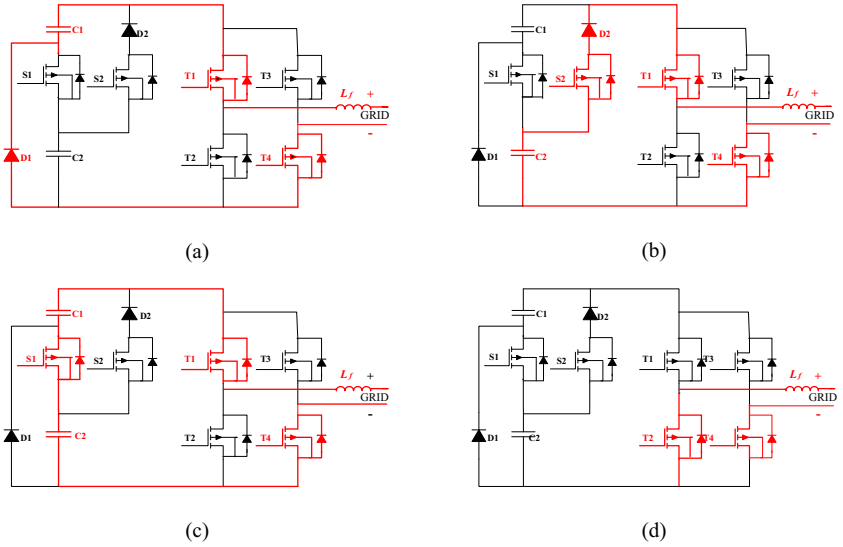

*Red line indicates the conduction of the switches and current direction

Fig. 6. Operational equivalent circuit diagram of seven-level inverter for upper half cycle, (a) *case 1*, (b) *case 2*, (c) *case 3*, and (d) *case 4*.

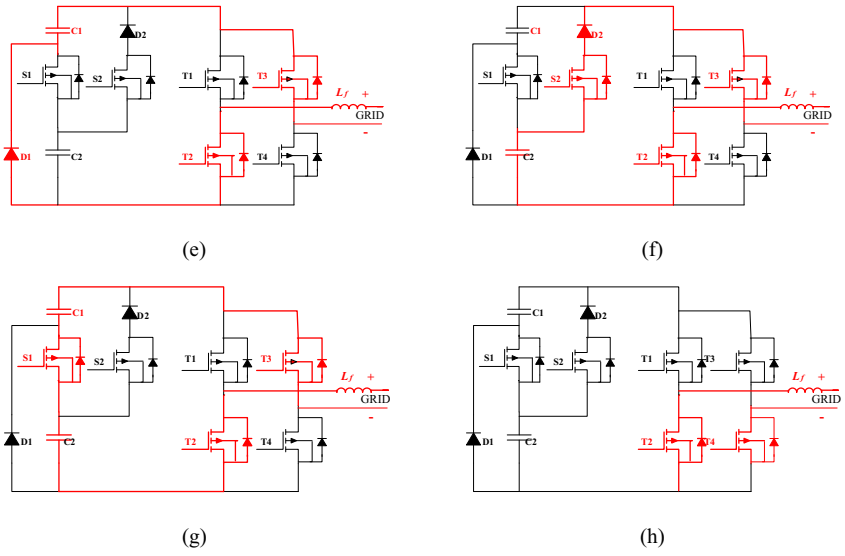

*Red line indicates the conduction of the switches and current direction

Fig. 7. Operational equivalent circuit diagram of seven-level inverter for lower half cycle, (e) *case 5*, (f) *case 6*, (g) *case 7*, and (h) *case8*.

For upper half cycle (+ve):

Case1-In this operational case as shown in Fig. 6(a), both the S1 and S2 switch are OFF, so that the capacitor C_1 discharge the current through D_1 and the diode is short at the same time. The output voltage of the capacitor is $\frac{V_{dc}}{3}$. During this operation, the power electronic switch T_1 and T_4 of the voltage source inverter are ON condition. At that time, RSCI output voltage is equal to the capacitor selection output voltage, which indicates that RSCI output voltage is $\frac{V_{dc}}{3}$.

Case2-In this operational case as shown in Fig. 6(b), the switch S_1 is OFF and S_2 is ON condition, so the capacitor C_2 has discharged the current through S_2 and D_2, at that time S_2 and D_2 are short. Due to this condition, the capacitor output voltage is $\frac{2V_{dc}}{3}$. Here, also the switch T_1 and T_4 are ON condition at the same time as in the previous case. Therefore, RSCI output voltage is $\frac{2V_{dc}}{3}$.

Case3-In this operational case as shown in Fig. 6(c), the switch S_1 is ON condition. Due to the S_1 is ON, the D_2 is reverse biased. The switch S_2 cannot oppose the current flow as it is ON condition during that period. To avoid the switching of S_2, the switch may be ON or OFF. In this case, the capacitor C_1 and C_2 are discharged at the same time and gives the output voltage V_{dc}. As in the previous case, the switch T_1 and T_4 are ON during this time.

Case4-In this operational case as shown in Fig. 6(d), both the switch S_1 and S_2 are OFF condition, and the capacitor output voltage is $\frac{V_{dc}}{3}$. In this case as T_4 is ON, therefore the positive output current of the RSCI passes through the filter inductor. To do a continuous conduction of filter inductor (L_f) current, the anti-parallel diode of the switch T_2 is needed to be ON condition. At that time RSCI voltage is zero.

After studying the above cases, the RSCI output voltage produced in upper half cycles are $\frac{V_{dc}}{3}$, $\frac{2V_{dc}}{3}$, V_{dc} and zero respectively. Like the upper half cycle (+ve), in the lower half cycle (−ve) also the output voltage of RSCI is same but has opposite sign. The Operational equivalent circuit diagram of seven-level inverter for lower half cycle of (e) *case 5*, (f) *case 6*, (g) *case 7*, and (h) *case 8* are illustrated in Fig. 7.

In the lower half cycle, the operation of the RSCI also further divided into 4 cases. By comparing Figs. 6 and 7 the capacitor selection circuit is same for both of the half cycle and one difference is instead of T_1 and T_4, T_2 and T_3 are on condition for three cases 5, 6 and 7. The last 8th case T_2 is on, and for a continuous conduction of the inductor current, the anti parallel diode of the switch T_4 is on. After completing both the cycle, the inverter gives seven voltage levels like: $\pm\frac{V_{dc}}{3}$, $\pm\frac{2V_{dc}}{3}$, $\pm V_{dc}$, and zero respectively.

The conduction of switches at RSCI is controlled by space vector pulse width modulation (SVPWM) technique [21,22]. The three-level inverter operates like a two-level inverter. As illustrated in Fig. 5, this design contains one voltage source inverter and two other switches named as S1 and S2 used to operate the VSI. In addition to that, other two capacitors and diodes are also used. Fig. 8 demonstrates the circuit diagram of the three-phase RSCI by adding two extra switches (T_5, T_6). The switches are conducted by varying the conduction angle. Tables 1 and 2 contain all the switching states sequentially for both upper and lower half cycles.

According to the utility side requirement, RSCI must be switched into two levels. In order to increase the filter current, one of the voltage levels is higher than the utility voltage and in order to decrease the filter current, another voltage level is lower than the utility voltage. In the above way, the output current of RSCI can be controlled to trace the reference current.

2.3. Design of LCL filter

To mitigate the harmonics produced by the inverter and nonlinear loads, LCL filter is designed according to the system requirement [37,38].

Apply KVL to the equivalent circuit diagram of LCL filter as illustrated in Fig. 9 [37]:

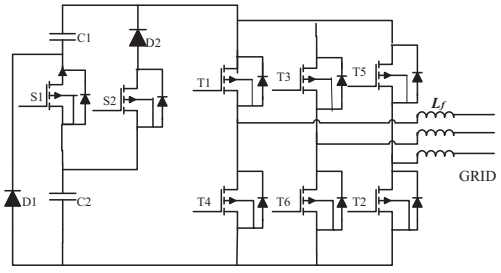

Fig. 8. Circuit diagram of three phase RSCI.

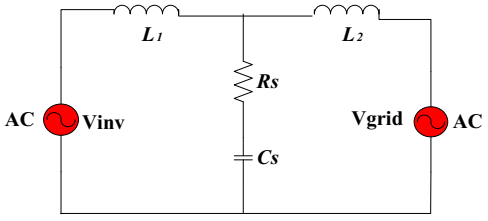

Fig. 9. Circuit diagram of LCL filter.

Table 1
For upper half cycle (+ve): (3 phase) switching states.

S_1	S_2	T_1	T_3	T_5	T_4	T_6	T_2	Vout(+)
✗	✗	✓	✗	✗	✗	✓	✓	$\frac{V_{dc}}{3}$
✗	✓	✓	✗	✗	✗	✓	✓	$\frac{2V_{dc}}{3}$
✓	✗	✓	✗	✗	✗	✓	✓	V_{dc}
✗	✗	✗	✗	✗	✗	✗	✓	Zero

Table 2
For lower half cycle (−ve): (3 phase) switching states.

S_1	S_2	T_1	T_3	T_5	T_4	T_6	T_2	Vout(−)
✗	✗	✗	✓	✓	✓	✗	✗	$\frac{V_{dc}}{3}$
✗	✓	✗	✓	✓	✓	✗	✗	$\frac{2V_{dc}}{3}$
✓	✗	✗	✓	✓	✓	✗	✗	V_{dc}
✗	✗	✗	✗	✓	✗	✗	✗	Zero

*'✓' and '✗' represents the switch ON and OFF condition respectively.

$$V_{inv} = V_{grid} + L\frac{dI_{inv}}{dt} = V_{grid} + L\frac{dI_{grid}}{dt} \tag{8}$$

$$I_{grid} = \frac{1}{L}\int (V_{inv}^{ref} - V_{grid})dt + \frac{1}{L}\int (V_{inv}^{h})dt \tag{9}$$

$$I_{grid}^{h} = \frac{1}{L}\int -2(\mathrm{sgn}I_{inv})\frac{t_d V_{dc}}{T_{sw}} \tag{10}$$

where I_{grid}, I_{grid}^{h}, t_d, and T_{sw} denote grid current (A), grid harmonic current (A), delay time (s), and switching time (s) respectively. The design parameters L_1, L_2, R_s and C_s of LCL filters are computed by line to line inverter output voltage (V_{LL}) in 'V', phase to phase voltage (V_{ph}) in 'V', rated active power (P_r) in 'W', dc link voltage (V_{dc}) in 'V', grid frequency (F_{grid}) in 'Hz', switching frequency (F_{sw}) in 'Hz', resonant frequency (F_{res}), and the grid angular frequency (ω_{grid}). By taking the above parameters, the base impedance (Z_b) and capacitance (C_b) are calculated as:

$$Z_b = \frac{V_{LL}^2}{P_r} \tag{11}$$

$$C_b = \frac{1}{\omega_{grid} Z_b} \tag{12}$$

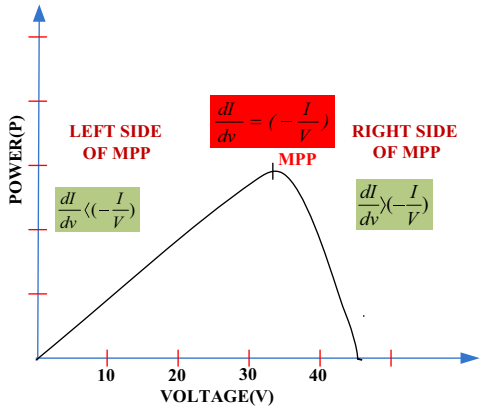

Fig. 10. slope diagram of IC method.

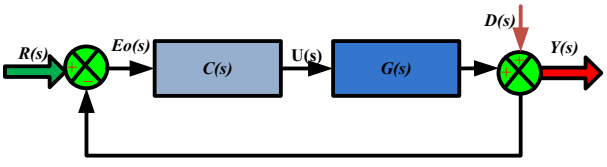

Fig. 11. Closed loop control of RSCI.

The capacitor size (C_s) is calculated in terms of base capacitance as:

$$C_s = 0.01/(0.05 \times C_b) \tag{13}$$

Here in Eq. (14), for designing the filter capacitor, the power factor variation of the grid is assumed within 5%. The maximum current ripple ($\Delta I_{L,\max}$) at RSCI is expressed as:

$$\Delta I_{L,\max} = \frac{2V_{dc}}{3L_1}(1-m)m \times T_{sw} \tag{14}$$

where L_1, and m denote the inverter side filter, and modulation index of SVPWM respectively.

Considering the value of m as 0.5, the maximum current ripple can be computed referring to Eq. (14) as:

$$\Delta I_{L,\max} = \frac{V_{dc}}{6F_{sw}L_1} \tag{15}$$

To get the maximum ripple current, a 10% ripple of the rated current is taken into consideration for calculation of L_1.

$$\Delta I_{L,\max} = 0.1 I_{\max} \tag{16}$$

$$I_{\max} = \frac{P_r\sqrt{2}}{3V_{ph}} \tag{17}$$

$$L_1 = \frac{V_{dc}}{6F_{sw}\Delta I_{L,\max}} \tag{18}$$

The LCL filter is designed to reduce the expected current ripple to 20% and considering that the'L_2' is determined in terms of the desired attenuation factor 'K_a' as follows:

$$L_2 = \frac{\sqrt{\frac{1}{K_a^2}+1}}{C_s\omega_{sw}^2} \tag{19}$$

To prevent the system from resonance condition, the resistor 'R_s' is combined with the capacitor and also responsible for reduction of ripple on the switching frequency. The 'R_s' value is computed as:

$$R_s = \frac{1}{3\omega_{res}C_s} \tag{20}$$

where $\omega_{res} = \sqrt{\frac{L_1+L_2}{L_1L_2C_s}}$

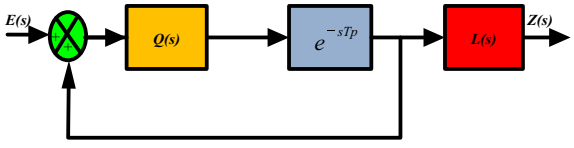

Fig. 13. Block diagram of RC controller.

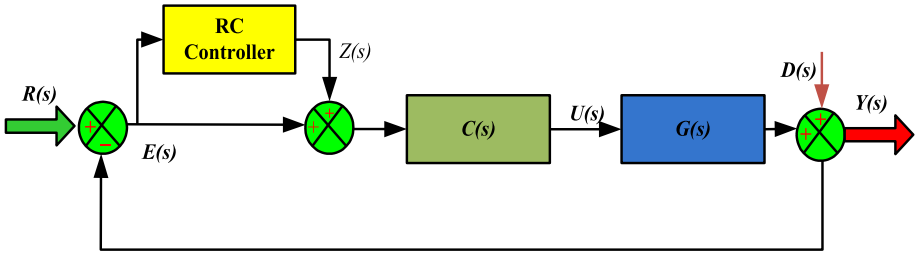

Fig. 12. Block diagram of controlled loop by using RC controller.

Table 3
System parameters.

Solar system data (1000 W/m^2, 25 + 273 K)	
Characteristic	Specifications
Typical max power (P_{max})	210.1 W
Voltage at max power (V_{max})	37.5 V
Current at max power (I_{max})	5.602 A
Short-circuit current (I_{sc})	6.04 A
Open circuit current (V_{oc})	44 V
Series resistance(R_s)	0.221 Ω
Parallel resistance(R_p)	415.405 Ω
Boltzmann constant(K)	$1.38065 * 10^{-23}$ J/K
Charge of electron (q)	$1.602 * 10^{-11}$ C
Material band gap (*Eg,ref*) for silicon cell	1.12 eV
ideality factor (a)	1.3 eV
Temperature coefficient of short-circuit current (*Ki*)	0.0032 A/K
LCL filter data	
Characteristic	Specifications
Line to line inverter output voltage (V_{LL})	143.66 V
Phase to phase voltage (V_{ph})	117.3 V
Rated active power (P_r)	558 W
Switching frequency (F_{sw})	$40 * 10^3$ Hz
Battery data	
Characteristic	Specifications
Battery voltage (V_{bat})	60 V
Battery inductor (L_{Bat})	5 mH

3. Control techniques

In this section, various control strategies incorporated in the present study are presented. For extracting the optimum power, an MPPT control algorithm based on IC method is adapted. A feedback control strategy based on d-q axis composition is also implemented for battery power management to enhance the efficiency and control of the system. Furthermore, a repetitive control strategy is applied with an objective to eliminate the harmonic distortion in space vector pulse width modulation.

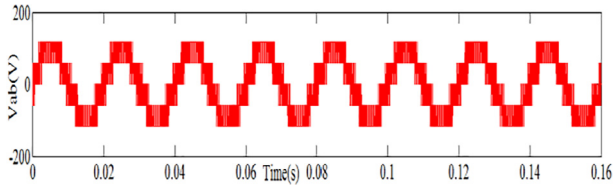

Fig. 14. Voltage of a three level inverter (NPC).

3.1. Incremental conductance (IC) based MPPT algorithm

By comparing the PV array impedance with inverter effective impedance reflected across the array terminal, the maximum power point (MPP) is traced in the IC method. An iterative approach is followed through choosing an optimal value of the increment factor or duty cycle 'M' [17]. Fig. 10 demonstrates the slope diagram of the IC method. For the IC method, the slope of the PV array power characteristics is followed and it is based on the concept that the slope of the PV array power curve is zero at the point of maximum power, positive for values of output power smaller than MPP and negative for the value of output power greater than MPP [18,19].

The algorithm is formulated, by differentiating the PV output power with respect to voltage and making it zero according to the condition to achieve MPP.

$$\frac{dp}{dV} = \frac{d}{dV}(VI) = I + V\frac{dI}{dV} = 0 \tag{21}$$

The above equation leads to approximately,

$$\Rightarrow \frac{dI}{dV} \cong \frac{\Delta I}{\Delta V} = -\frac{I_m}{V_m} \tag{22}$$

where, 'I_m' and 'V_m' indicate the current and voltage at MPP. This indicates the operating point position can be evaluated, whether it is far or near to MPP. So judiciously calculating the increment 'M', the operating point can be approached to MPP. Mathematically, the whole process at voltage source region and current source region can be represented as follows:

$$\frac{dI}{dV} < -\frac{I}{V} \Rightarrow M = M + \Delta M \text{ (Left side MPP)} \tag{23}$$

$$\frac{dI}{dV} > -\frac{I}{V} \Rightarrow M = M - \Delta M \text{ (Right side MPP)} \tag{24}$$

$$\text{At MPP}, \frac{dI}{dV} = -\frac{I}{V} \Rightarrow M = M \tag{25}$$

3.2. Control of battery energy management

By the network supervisory block as illustrated in Fig. 1, the desired active and reactive power generation for the utility sector

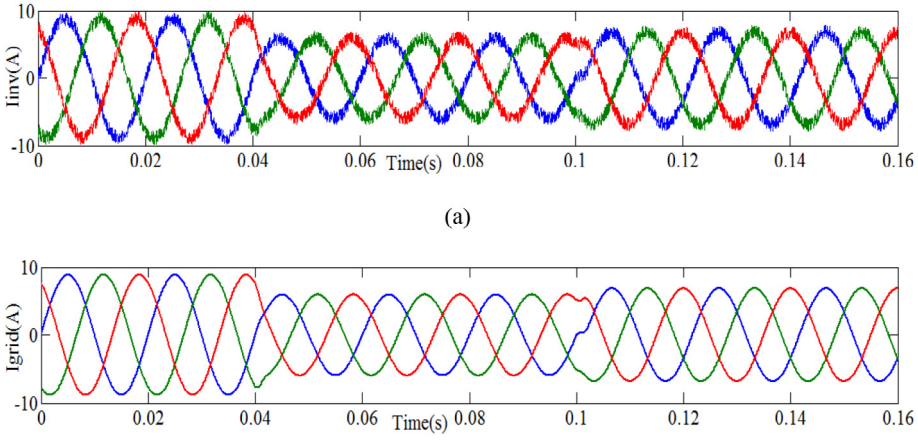

Fig. 15. (a) Output current of NPC inverter (b) Output current of grid.

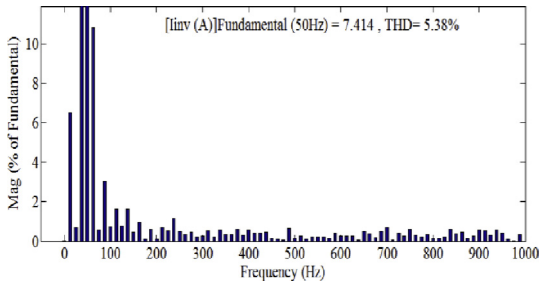

Fig. 16. THD calculation of inverter side current.

is regulated by the proposed inverter (RSCI) control. The above conditions will be attained by considering the solar parameters, grid parameters and the battery parameters. Using Park's transformation, the active power (p) in 'W' and reactive power (q) in 'VAR' can be expressed in terms of d-q axis voltage and current components [1].

$$p = V_{sd}I_d + V_{sq}I_q \tag{26}$$

$$q = V_{sq}I_d - V_{sd}I_q \tag{27}$$

where 'V_{sd}' and 'V_{sq}' represent the d-q axis grid voltages (V); 'i_d' and 'i_q' represent the corresponding inverter current (A) in the d-q axis. The corresponding d and q axis inverter current can be derived in terms of desired active and reactive power (p^* and q^*) using Eqs. (26), (27) as follows:

$$i_d = \frac{p^*V_{sd} - q^*V_{sq}}{V_{sd}^2 + V_{sq}^2} \tag{28}$$

$$i_q = \frac{q^*V_{sd} - p^*V_{sq}}{V_{sd}^2 + V_{sq}^2} \tag{29}$$

The inverter desired voltage vector is computed by applying decoupled control strategy and implemented through a RC controller. The battery operates in two modes of operation for transforming a specified amount of power. In charging mode, the battery will receive the power from the PV's available surplus

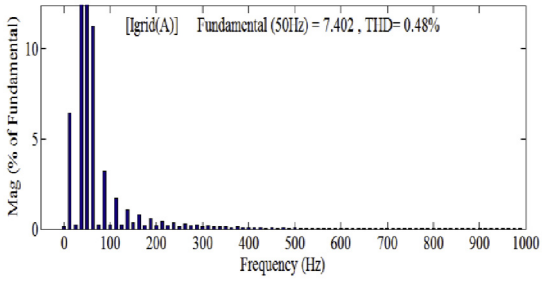

Fig. 17. THD calculation of grid side current.

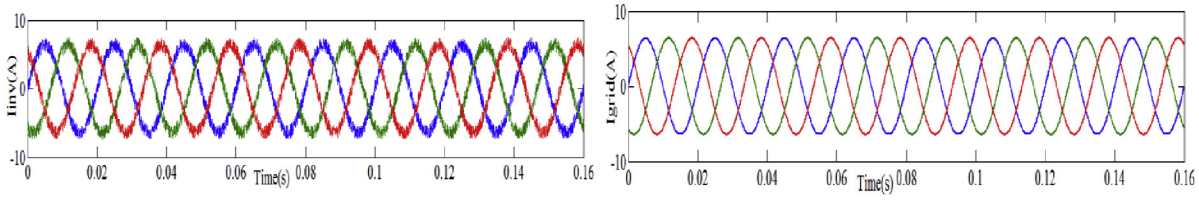

(a) (b)

Fig. 18. (a) Output current of inverter (b) Output current of grid.

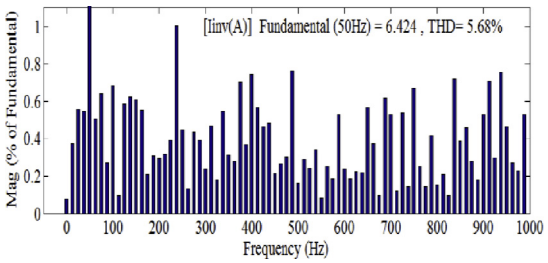

Fig. 19. THD calculation of inverter side current.

energy. In the discharging mode of operation, it supports the PV system when unable to supply the required power. The battery function in this study plays a role of auxiliary support to enhance the reliability and efficiency of PV operation by utilizing the surplus power during the deficiency.

The proposed battery energy control management of the test system is illustrated in Fig. 1. In this control topology the battery will absorb power when an excess amount of power is available in the grid and similarly supply power when the grid cannot support the desired power. The calculated reference voltage vector is further used to determine the appropriate sector in the vector diagram. The shortest vector is needed to be rightly chosen by the relative errors of capacitor voltages as in Eqs. (30), (31).

$$eV_{Ca} = \frac{V_{Ca}^* - V_{Ca}}{V_{Ca}} \tag{30}$$

$$eV_{Cb} = \frac{V_{Cb}^* - V_{Cb}}{V_{Cb}} \tag{31}$$

where V_{Ca}^* and V_{Cb}^* denote the desired capacitor voltage (V), V_{Ca} and V_{Cb} denote the actual capacitor voltage (V) across the capacitor 'Ca' and 'Cb' respectively [23].

The shortest vector selection through this approach as explained above are used to determine the selection of capacitor to be in charging mode or in discharging mode of operation. The decision to select the right short vector mostly depends on the relative short vector, relative errors of capacitor voltages and their importance on the control system behavior. Taking this idea a decision function 'E' is formulated as follows:

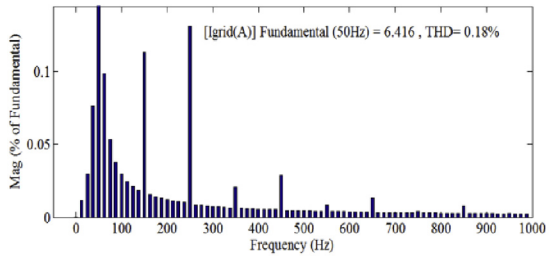

Fig. 20. THD calculation of grid side current.

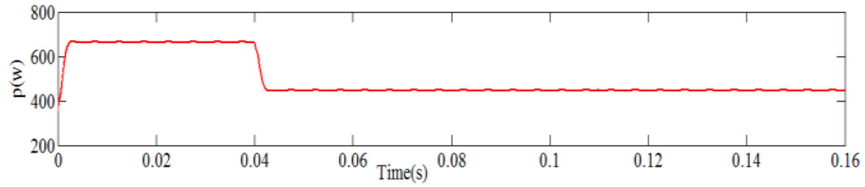

(a)

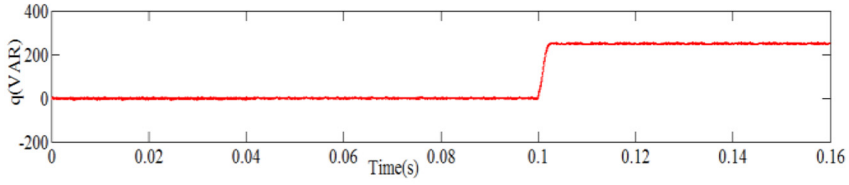

(b)

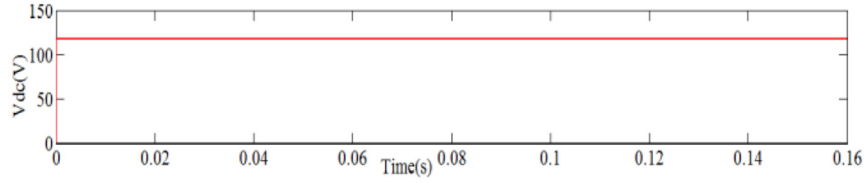

(c)

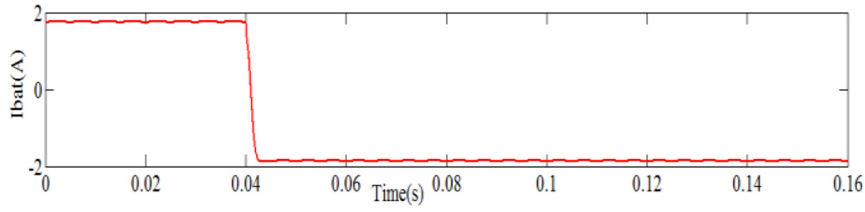

(d)

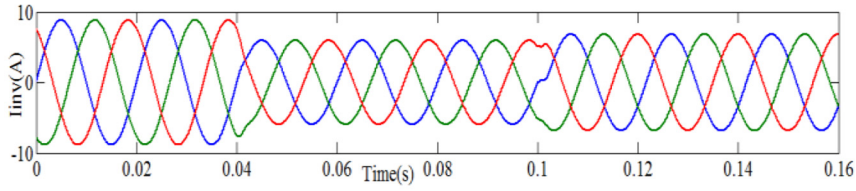

(e)

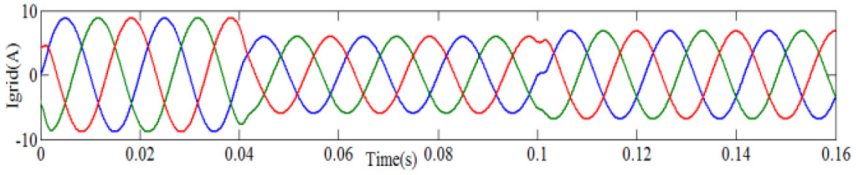

(f)

Fig. 21. By fixed irradiance: (a) active power (b) reactive power (c) PV output voltage (d) charging and discharging of battery (e) output current of inverter (f) output current of grid.

$$E = K_1 eV_{Ca} - K_2 eV_{Cb} \quad (32)$$

Each relative errors of the capacitor voltage are combined with the gains 'K_1' and 'K_2' values to determine the decision function. The associated gains 'K_1' and 'K_2' values are decided such a way that the corresponding relative error of the capacitor voltage allows better control of the chosen capacitor voltage. The corresponding values of 'K_1' and 'K_2' need to have the same reference voltage to balance the capacitor voltage. However, in this application, it is suggested to use different K_1 and K_2 values completely dependent on their desired capacitor voltages in case of the unbalanced capacitor voltage applications. The photovoltaic system is controlled by the IC method and '*Ca*' voltage is controlled to permit the battery charging and discharging by using the Eqs. (33) and (34).

$$V^*_{Ca} = V_{bat} \quad (33)$$

$$V_{ref} - V_{Ca} = V^*_{Cb} \quad (34)$$

In every time step, the selections of short vectors depend upon the polarity of '*E*'. In case of positive sign of '*E*' in any time step, the corresponding short vector selection can charge '*Ca*' or discharge '*Cb*' according to the equations. Similarly, in case of negative sign of '*E*', the corresponding short vector selection can charge '*Cb*' or discharging '*Ca*' during that time step.

According to the proposed control system as illustrated in Fig. 1, by using the desired voltage vector and the corresponding actual timing of the applied voltages, the desired active power (p^*) and reactive power (q^*) are produced by the RSCI. Furthermore, an attempt has been made on the generation side by MPPT control to achieve robust control of V_{Cb} ($K_2 \gg K_1$) with reference value of ($V^*_{dc} - V_{Ca}$). Along with that V_{Ca} is flexibly controlled with the battery voltage reference value 'V_{bat}' [29].

The proper short voltage vector can be determined to implement the requested voltage vector by using the decision function '*E*' along with the given reference values. Through the optimal MPPT control, the system can generate maximum available power (P_{pv}). In addition to that by generating the desired voltage vector in grid side, it is possible to meet the desired power (p^*) at the grid. The proposed control system also automatically controls V_{Ca}, such that the excess power is supplied to the battery and during the power deficit the power absorbs from the battery storage.

In the proposed system the battery inductor is used for smoothen the battery current, mainly during the disturbance conditions. For the operation, a wide range of the inductor value can be chosen, but decreasing the inductor value will increase the overshoot of the battery and also this value totally depends on the capacitor value and the fluctuation of the voltage. The size and cost point of view, the value of the inductor is chosen as 5 mH.

3.3. Repetitive controller

The repetitive control (RC) strategy on frequency domain is presented here. It is designed and analyzed based on discrete time Fourier transforms in Z domain [30,31]. The block diagram repre-

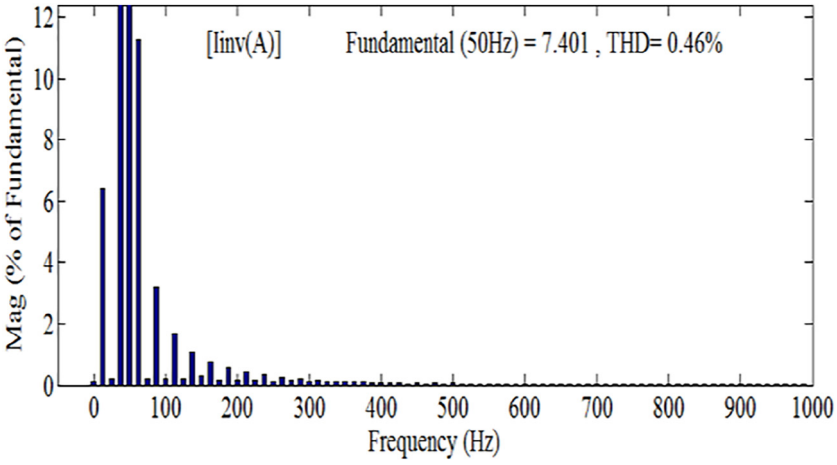

Fig. 22. THD calculation of inverter side current.

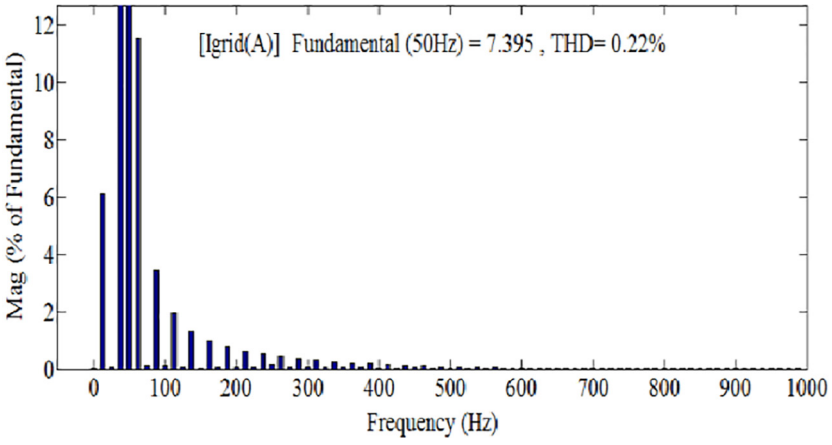

Fig. 23. THD calculation of grid side current.

sentation of closed-loop feedback controller of RSCI is illustrated in Fig. 11. Disturbances generated by any means like non-linear loads, fluctuation in power system and nonlinear delay time, generates some lower order harmonics in the practical system. By using conventional LC and LCL filter, it is not sufficient to eliminate the lower order harmonics that tend to inject high THD in the output waveforms

To minimize the lower order harmonics and getting better output voltage on the grid side, it is necessary to design an appropriate controller. The state space model representation of the system can be represented as:

$$Y(s) = G(s) * U(s) + D(s) \tag{35}$$

$$U(s) = C(s) * R(s) - Y(s) \tag{36}$$

As shown in Fig. 12, where $R(s)$ is the reference input signal, $C(s)$ is the controller, $G(s)$ is the inverter, $D(s)$ is the disturbance, and $Y(s)$ is the output of the closed loop system. The tracking error $E_0(s)$ of the closed loop system due to the control input $U(s)$ and $D(s)$ is given by:

$$E_0(s) = \frac{R(s) - D(s)}{1 + C(s)G(s)} \tag{37}$$

The Fig. 12 shows the RC controller implementation with the closed loop system model. The tracking error is modified further by the RC controller before feeding to the main system controller. Fig. 13 demonstrates the topology of RC controller. The filter '$L(s)$' act as a learning filter to compensate the transfer as seen by RC controller. The function of the '$Q(s)$' filter is used to minimize the error between '$L(s)$' and error in the real system [32–36].

Furthermore, '$Q(s)$' try to limit the frequency within the specified boundary of the RC controller. The phase delay of '$Q(s)$' can be compensated by adjusting the time delay e^{-STp} of the periodic signal generator. The function of RC controller in case of the periodic signal is to generate the output frequencies with multiple of integer and periodic frequency as $k\omega_p$. The time period T_p can be computed as:

$$T_p = \frac{2\Pi}{\omega_p} \tag{38}$$

The closed loop transfer function can be represented as:

$$H(s) = \frac{C(s)G(s)}{1 + C(s)G(s)} \tag{39}$$

Similarly to represent the tracking error '$E(s)$' of the RC controller in terms of the tracking error '$E_0(s)$' of the original system without RC can be expressed as:

$$E(s) = E_0(S) \times \frac{1 - Q(s)e^{-ST_p}}{1 - ([1 - L(s)] \times Q(s)e^{-ST_p})} \tag{40}$$

4. Results

A simulation model is built in MATLAB to test and validate the effectiveness of the proposed approach. Comparative results are presented and analyzed under fixed and variable irradiance condition among three-level neutral point clamped (NPC) inverter with PI controller and RSCI with the repetitive controller. The simulated parameter of the proposed system is illustrated in Table 3.

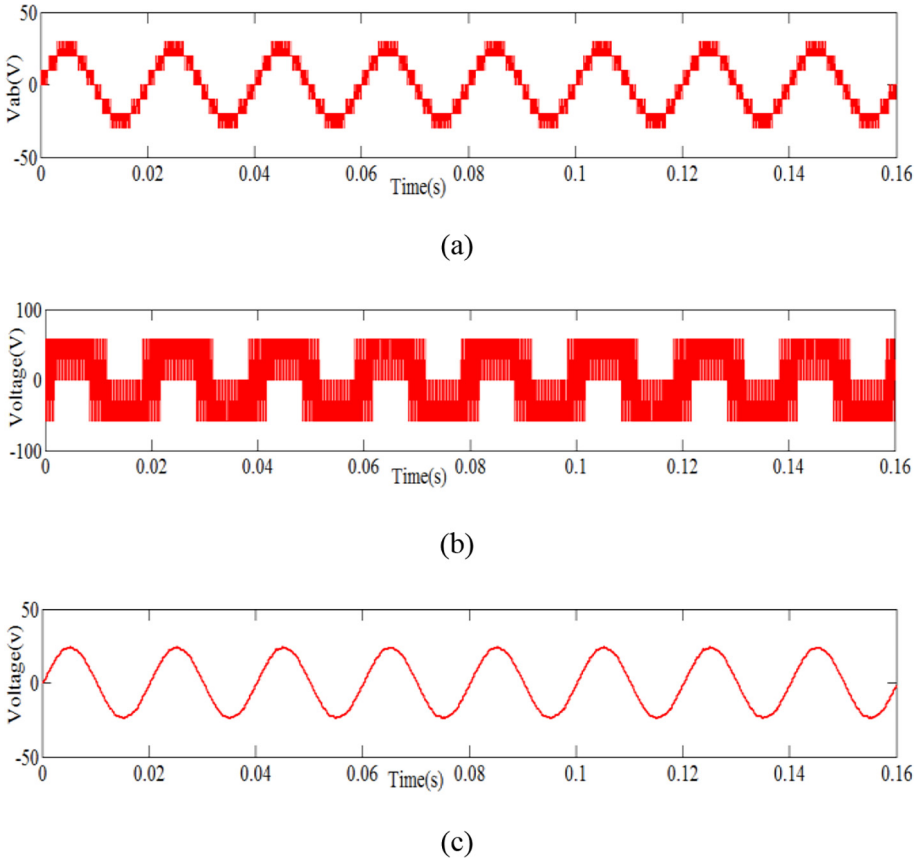

Fig. 24. By fixed irradiance: (a) phase to phase voltage of inverter (b) phase voltage of inv due to mid point (c) Filtered phase voltage of inverter w.r.t midpoint.

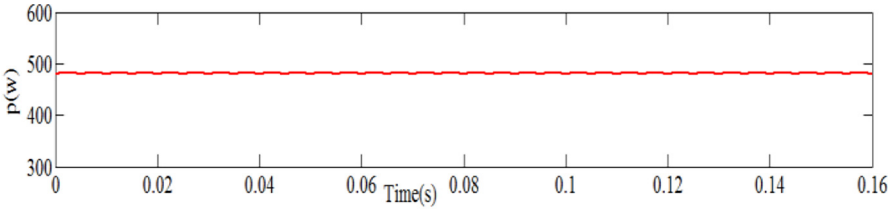

(a)

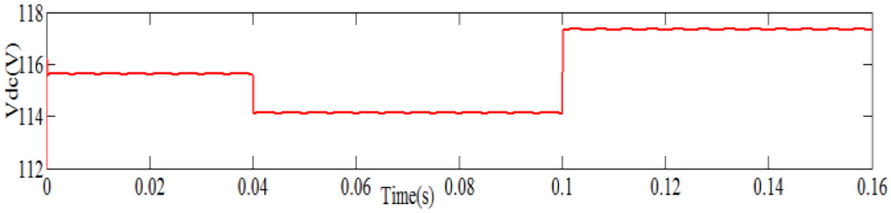

(b)

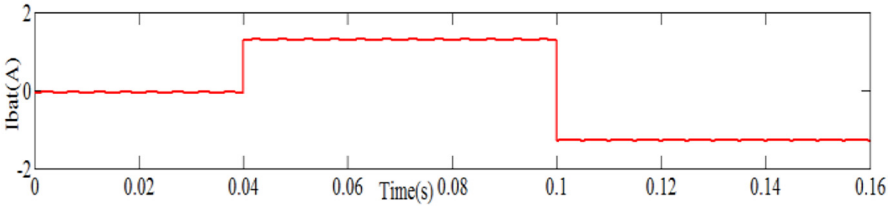

(c)

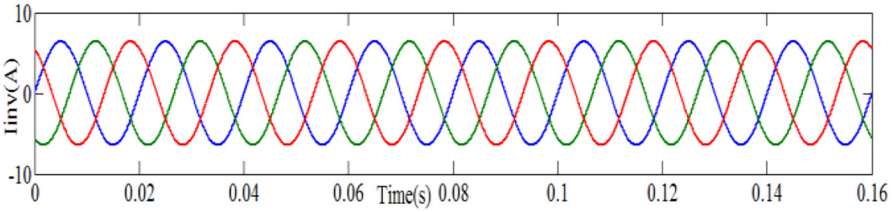

(d)

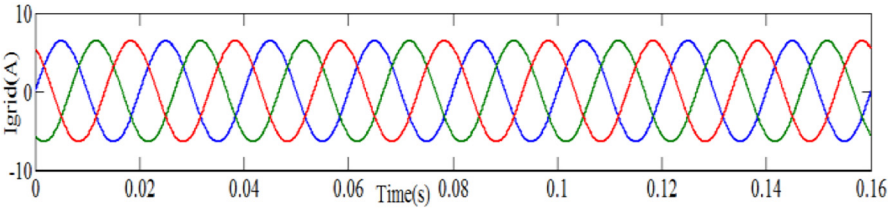

(e)

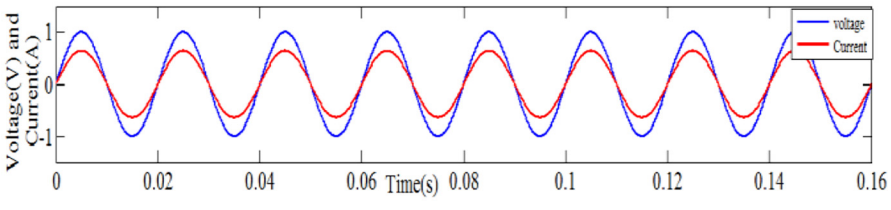

(f)

Fig. 25. By varying the irradiance: (a) active power (b) PV output voltage (c) charging and discharging of battery (d) inverter output current (e) output current of grid (f) phase-a grid voltage and current.

4.1. Case1: Three-level neutral point clamped (NPC) inverter with PI controller

4.1.1. Fixed irradiance condition

The NPC MLI topology to generate the required voltage level, it comprised with four power electronic switches and two clamping diodes in one leg and so totally it contains 12 switches, 6 clamping diodes, and two capacitors [10,11]. Considering this topology with PI controller, the system generates the required inverter output current and grid current. Fig. 14 demonstrates the positive, negative and zero sequence voltage components adapting this approach.

The output current at inverter and grid side bus are illustrated in Fig. 15. This result in Fig. 15(a) in case of inverter current indicates harmonic distortions and that have been removed by the integrated LCL filter as shown in Fig. 15(b). Figs. 16,17 shows the harmonic assessment for the inverter current for four cycles at 50 Hz fundamental frequency through Fast Fourier Transform (FFT) analysis. The 5.38% THD is too high according to the IEEE 1541 standard and so it needs a further improvement for real-time implementation particularly for PV based microgrid. The use of LCL filter plays a vital role in improving the above power quality issues by reducing the THD level from 5.38% to 0.48% as shown in Fig. 17 (Fig. 16).

4.1.2. Varying irradiance condition

The performance of the LCL filter is tested for the same system under varying irradiance condition. Fig. 18 shows the simulation results of the grid side and inverter side current. The results from Fig. 18(a) clearly indicate the harmonic distortion in case of inverter current due to the presence of nonlinearity in the inverter. However, the effectiveness of using LCL filter to reduce harmonics level for the above power quality issue is reflected in the grid side current as illustrated in Fig. 18(b). This analysis has been confirmed by calculating THD level in the inverter side current by using the FFT technique for 4 cycles at 50 Hz fundamental frequency. Figs. 19 and 20 indicate a high reduction of THD value from 5.68% to 0.18% by implementing the LCL filter. From the findings of the above results, the limitation like a need of LCL filters to generate three level voltage and that to the design of MLI with more number of switches for the operation are reflected. This motivates to design the reduced switch MLI with less dependency on integrated filter model, by taking the above limitations in the proposed approach.

4.2. Case2: CSIR with repetitive controller

4.2.1. Fixed irradiance condition:

Fig. 21 shows the time variation of active power, reactive power, PV output voltage, and output current of the inverter, an output current of the grid, and charging and discharging of battery current. In the system there are three PV units are connected in series to make a PV module. In this study, it is assumed that the irradiation will produce I_{ph} = 5.6 A in the rated PV system and producing the voltage output is $117.3V_{dc}$ and the current output is given 4.75 A. Finally, the total active power of 558 W is generated,

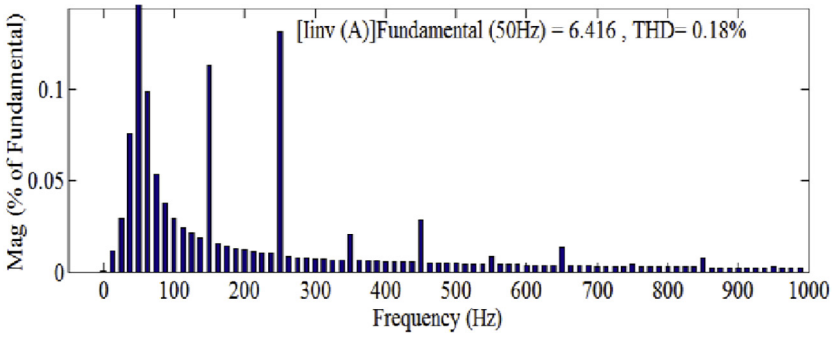

Fig. 26. THD calculation of Inverter side current.

Table 4
Inverter current harmonic current analysis between three-level and seven-level inverter (Fixed irradiance).

Inverter harmonic current analysis (Fixed irradiance)							
FFT analysis reports of three-level inverter with PI controller				FFT analysis reports of seven-level inverter with RC controller			
Total harmonic distortion (THD) = 5.38%				Total harmonic distortion (THD) = 0.46%			
Order of Harmonics	Frequency (HZ)	% of harmonics	Angle in degree	Order of Harmonics	Frequency (HZ)	% of harmonics	Angle in degree
0	0	0.03	90	0	0	0.11	90
1	50	100	0	1	50	100	0.1
2	100	0.73	79.9	2	100	0.20	59.2
3	150	0.46	267.8	3	150	0.29	39.8
4	200	0.11	242.2	4	200	0.17	16.6
5	250	0.48	0	5	250	0.11	40.3
6	300	0.25	39.8	6	300	0.13	0
7	350	0.35	29.7	7	350	0.12	0
8	400	0.58	167.5	8	400	0.08	0
9	450	0.14	0	9	450	0.05	0
10	500	0.14	51.6	10	500	0.05	0
11	550	0.21	34.2	11	550	0.03	0
12	600	0.25	222.2	12	600	0.03	262.2
13	650	0.50	204.0	13	650	0.03	235.5
14	700	0.68	122.1	14	700	0.02	240.4
15	750	0.60	94.2	15	750	0.01	257.7

Table 5
Inverter current harmonic current analysis between three-level and seven-level inverter (Varying irradiance).

Inverter harmonics current analysis (Changing irradiance)							
FFT analysis reports of three-level inverter with PI controller				FFT analysis reports of seven-level inverter with RC controller			
Total harmonic distortion (THD) = 5.68%				Total harmonic distortion (THD) = 0.18%			
Order of Harmonics	Frequency (HZ)	% of harmonics	Angle in degree	Order of Harmonics	Frequency (HZ)	% of harmonics	Angle in degree
0	0	0.08	270	0	0	0	270
1	50	100	0	1	50	100	0
2	100	0.69	75.8	2	100	0.03	180.2
3	150	0.61	258.4	3	150	0.11	51.5
4	200	0.29	244.1	4	200	0.01	180.7
5	250	0.45	8.8	5	250	0.13	138.7
6	300	0.24	76.5	6	300	0.01	182.3
7	350	0.31	80.2	7	350	0.02	58.6
8	400	0.74	158.1	8	400	0.01	182.4
9	450	0.21	0	9	450	0.03	143.7
10	500	0.16	105.6	10	500	0	183.2
11	550	0.08	0	11	550	0.01	66.5
12	600	0.24	234.3	12	600	0	183.2
13	650	0.56	217.9	13	650	0.01	148.0
14	700	0.53	142.2	14	700	0	185.2
15	750	0.67	98.0	15	750	0	74.1

which varies initially in the range of 662 W to 445 W up to time interval t = 40 ms as shown in Fig. 21(a). Fig. 21(b) similarly indicates the reactive power variation and shows the initial variation of reactive power transmitted to the grid from zero to 250 VAR during a time interval t = 100 ms. Due to the presence of capacitor, the system is able to generate the requested reactive power. Fig. 21 (c) shows the output dc voltage variation of the PV module. A battery energy management is essential to improve the efficiency and reliability in case of a PV based microgrid. The control strategy and planning are to be implemented to charge the battery during the peak period and discharge the battery energy to meet the deficit of power. The time variation of battery power utilization is shown in Fig. 21(d). During the battery discharging operation the current rating reaches 1.9 A during the time interval 0–40 ms and during charging condition the current reaches −1.9 A during the time interval 40 ms–100 ms.

The effectiveness of the proposed approach is illustrated in Fig. 21(e–f) in terms of minimization of harmonics and transfers the system characteristics almost to a linear behavior. This indicates the less dependency on LCL filter as compared to case-1 three-level NPC inverter. The FFT analysis clearly indicates this by showing a reduced level of THD of 0.46% that to without the use of LCL filter as illustrated in Fig. 22. However, in Fig. 23a further enhanced performance is achieved by the use of LCL filter with THD level grid side current to 0.22%. The integration of LCL filter is considered in the proposed approach due to its system protection benefit under sudden change of voltage.

Fig. 24 shows the time variation of phase to phase voltage of inverter, phase voltage of inverter due to midpoint, and filtered phase voltage of inverter with respect to midpoint. The proposed RC controller based RSCI generates more voltage level as compare to the three-level neutral clamped inverter, illustrated in Fig. 24(a and b). The filtered phase voltage of proposed inverter with respect to midpoint is illustrated in Fig. 24(c) with minimal harmonic distortion.

4.2.2. Varying irradiance condition

It is assumed that by changing the solar irradiation, the PV module will produce the short circuit current as 4.2 A, 3.5 A, and 5 A with a time interval of 0 s, 0.04 s, and 0.1 s respectively. The output voltages of the PV modules are $114.5V_{dc}$, $113.2V_{dc}$, and $116.04V_{dc}$, and the corresponding currents 3.7 A, 3.2 A, and 4.4 A are achieved respectively. The corresponding power of the system is obtained as 362.24 W, 423.65 W, and 510.52 W respectively and the average power is computed as 481.52 W. In this simulation study the range of active power is found to be within the range of 480 W to 482 W as illustrated in Fig. 25(a) and that meets the requisite power need to supply to grid. Fig. 25(b and c) shows the PV output dc voltage and the corresponding battery charging and discharging condition through battery current variation respectively. This indicates the battery energy management according to the integrated PV generation. If PV generation operates below the rated power to be supplied to the grid or during faulted operating condition, then the battery discharges to compensate the deficit power. Fig. 25(d) shows the inverter output current and Fig. 25(e) shows the grid side current with lower THD. Fig. 25(f) shows a single phase voltage and current in p.u conduction of the grid and its in-phase condition indicates zero reactive power at all time. The Fig. 26 shows THD level of the inverter side current by using FFT. The results clearly indicate a minimized harmonics level with THD value as 0.18% by using the proposed technique.

4.3. Case-3: Harmonic analysis

Table 4 presents inverter harmonic current analysis between three-level and proposed seven-level inverter under fixed irradiance condition. Similarly Table 5 shows the inverter harmonic current analysis between three-level and proposed seven-level inverter under varying irradiance condition. The THD value through FFT analysis for the proposed approach is 0.46% and 0.18% in case of fixed and varying irradiance condition on comparison to conventional three-level inverter as 5.38% and 5.68% respectively. The results indicate the existence of better power quality for the test system through the implementation of proposed approach.

5. Conclusion

This paper suggests a multilevel inverter based on RSCI for energy storage based PV microgrid system. In addition to that, an MPPT technique based on incremental conductance algorithm is applied to extract maximum available energy with fixed and different irradiance condition. To improve the performance further, a repetitive control strategy is implemented instead of PI controller along with RSCI. To ensure its possibility of real-time application, the harmonic levels are computed by finding THD value through

FFT analysis and found to be well within the IEEE-1547 standard. The integration of LCL filter is investigated for further improvement of power quality; even though the proposed approach gives a satisfactory result. Furthermore, the effectiveness of the battery to enhance the overall system performance is investigated through the proposed controller. The simulation results indicate the better performance of the proposed inverter topology and control strategy on compare to NPC inverter with PI controller in terms of better voltage level, reduce switches, negligible steady-state error and minimized harmonic level.

References

[1] M. Bragard, N. Soltau, S. Thomas, R.W. De Doncker, The balance of renewable sources and user demands in grids: power electronics for modular battery energy storage systems, IEEE Trans. Power Electron. 25 (12) (2010 Dec) 3049–3056.

[2] R. Banos, F. Manzano-Agugliaro, F.G. Montoya, C. Gil, A. Alcayde, J. Gómez, Optimization methods applied to renewable and sustainable energy: a review, Renew. Sustain. Energy Rev. 15 (4) (2011 May 31) 1753–1766.

[3] D. Rekioua, E. Matagne, Optimization of Photovoltaic Power Systems: Modelization, Simulation and Control, Springer Science & Business Media, 2012.

[4] J. Leuchter, V. Rerucha, A.F. Zobaa, Mathematical modeling of photovoltaic systems, in: Power Electronics and Motion Control Conference (EPE/PEMC), 2010 14th International 2010 Sep 6, IEEE, pp. S4-1.

[5] O.M. Toledo, D. Oliveira Filho, A.S. Diniz, Distributed photovoltaic generation and energy storage systems: a review, Renew. Sustain. Energy Rev. 14 (1) (2010 Jan 31) 506–511.

[6] T. Salmi, M. Bouzguenda, A. Gastli, A. Masmoudi, Matlab/simulink based modeling of photovoltaic cell, Int. J. Renew. Energy Res. (IJRER) 2 (2) (2012 May 12) 213–218.

[7] M.G. Villalva, J.R. Gazoli, E. Ruppert Filho, Modeling and circuit-based simulation of photovoltaic arrays, in: Power Electronics Conference, 2009. COBEP'09. Brazilian 2009 Sep 27, IEEE, pp. 1244–1254.

[8] M.G. Villalva, J.R. Gazoli, Filho E. Ruppert, Comprehensive approach to modeling and simulation of photovoltaic arrays, IEEE Trans. Power Electron. 24 (5) (2009 May) 1198–1208.

[9] W. De Soto, S.A. Klein, W.A. Beckman, Improvement and validation of a model for photovoltaic array performance, Solar Energy 80 (1) (2006 Jan 1) 78–88.

[10] B. Van Zeghbroeck, Principles of Semiconductor Devices, Colarado University, 2004.

[11] H.L. Tsai, C.S. Tu, Y.J. Su, Development of generalized photovoltaic model using MATLAB/SIMULINK, in: Proceedings of the world congress on Engineering and computer science 2008 Oct 22, vol. 2008, pp. 1–6.

[12] X. Zhang, Z. Shao, F. Wang, P. Liu, K. Ren, Zero-sequence circulating current reduction for three-phase three-level modular photovoltaic grid-connected systems, in: Zhongguo Dianji Gongcheng Xuebao (Proceedings of the Chinese Society of Electrical Engineering) 2013 Mar 25, Chinese Society for Electrical Engineering, vol. 33(9) pp. 17–24.

[13] H.R. Teymour, D. Sutanto, K.M. Muttaqi, P. Ciufo, Solar PV and battery storage integration using a new configuration of a three-level NPC inverter with advanced control strategy, IEEE Trans. Energy Convers. 29 (2) (2014 Jun) 354–365.

[14] O. Hachana, K.E. Hemsas, G.M. Tina, C. Ventura, Comparison of different metaheuristic algorithms for parameter identification of photovoltaic cell/module, J. Renew. Sustain. Energy 5 (5) (2013 Sep) 053122.

[15] S. Jain, V. Agarwal, Comparison of the performance of maximum power point tracking schemes applied to single-stage grid-connected photovoltaic systems, IET Electron. Power Appl. 1 (5) (2007 Sep 1) 753–762.

[16] A. Yazdani, A.R. Di Fazio, H. Ghoddami, M. Russo, M. Kazerani, J. Jatskevich, K. Strunz, S. Leva, J.A. Martinez, Modeling guidelines and a benchmark for power system simulation studies of three-phase single-stage photovoltaic systems, IEEE Trans. Power Delivery 26 (2) (2011 Apr) 1247–1264.

[17] M.A. Abdullah, A.H. Yatim, C.W. Tan, R. Saidur, A review of maximum power point tracking algorithms for wind energy systems, Renew. Sustain. Energy Rev. 16 (5) (2012 Jun 1) 3220–3227.

[18] D. Sera, L. Mathe, T. Kerekes, S.V. Spataru, R. Teodorescu, On the perturb-and-observe and incremental conductance MPPT methods for PV systems, IEEE J. Photovoltaics 3 (3) (2013 Jul) 1070–1078.

[19] T. Logeswaran, A. SenthilKumar, A review of maximum power point tracking algorithms for photovoltaic systems under uniform and non-uniform irradiances, Energy Proc. 1 (54) (2014 Jan) 228–235.

[20] X. Lin, S. Gao, J. Li, H. Lei, Y. Kang, A new control strategy to balance neutral-point voltage in three-level NPC inverter, in: Power Electronics and ECCE Asia (ICPE & ECCE), 2011 IEEE 8th International Conference on 2011 May 30, IEEE, pp. 2593–2597.

[21] J. Rodriguez, S. Bernet, P.K. Steimer, I.E. Lizama, A survey on neutral-point-clamped inverters, IEEE Trans. Ind. Electron. 57 (7) (2010 Jul) 2219–2230.

[22] A. Lewicki, Z. Krzeminski, H. Abu-Rub, Space-vector pulsewidth modulation for three-level NPC converter with the neutral point voltage control, IEEE Trans. Ind. Electron. 58 (11) (2011 Nov) 5076–5086.

[23] S. Burusteta, J. Pou, S. Ceballos, I. Marino, J.Á. Alzola, Capacitor voltage balance limits in a multilevel-converter-based energy storage system, in: Power Electronics and Applications (EPE 2011), Proceedings of the 2011-14th European Conference on 2011 Aug 30,IEEE, pp. 1–9.

[24] J. Pereda, J. Dixon, High-frequency link: a solution for using only one DC source in asymmetric cascaded multilevel inverters, IEEE Trans. Ind. Electron. 58 (9) (2011 Sep) 3884–3892.

[25] J. Chavarria, D. Biel, F. Guinjoan, C. Meza, J.J. Negroni, Energy-balance control of PV cascaded multilevel grid-connected inverters under level-shifted and phase-shifted PWMs, IEEE Trans. Ind. Electron. 60 (1) (2013 Jan) 98–111.

[26] J.C. Wu, C.W. Chou, A solar power generation system with a seven-level inverter, IEEE Trans. Power Electron. 29 (7) (2014 Jul) 3454–3462.

[27] I. Sefa, N. Altin, S. Ozdemir, O. Kaplan, Fuzzy PI controlled inverter for grid interactive renewable energy systems, IET Renew. Power Gener. 9 (7) (2015 Apr 7) 729–738.

[28] R. Nagarajan, A. Yuvaraj, V. Hemalatha, S. Logapriya, A. Mekala, S. Priyanga, Implementation of PV-based boost converter using PI controller with PSO algorithm, Int. J. Eng. Comput. Sci. 6 (3) (2017).

[29] F. Zaouche, D. Rekioua, J.P. Gaubert, Z. Mokrani, Supervision and control strategy for photovoltaic generators with battery storage, Int. J. Hydrogen Energy 42 (30) (2017 Jul 27) 19536–19555.

[30] M. Steinbuch, Repetitive control for systems with uncertain period-time, Automatica 38 (12) (2002 Dec 31) 2103–2109.

[31] S. Chen, Y.M. Lai, S.C. Tan, K.T. Chi, Optimal design of repetitive controller for harmonic elimination in PWM voltage source inverters, in: Telecommunications Energy Conference, 2007. INTELEC 2007. 29th International 2007 Sep 30, IEEE pp. 236–241.

[32] S. Jiang, D. Cao, Y. Li, F.Z. Peng, Grid-connected boost-half-bridge photovoltaic microinverter system using repetitive current control and maximum power point tracking, IEEE Trans. Power Electron. 27 (11) (2012 Nov) 4711–4722.

[33] Z. Shao, Z. Xiang, High-order repetitive control for discrete-time linear switched systems, Int. J. Syst. Sci. 48 (9) (2017 Jul 4) 1882–1890.

[34] Z. Shao, Z. Xiang, Iterative learning control for non-linear switched discrete-time systems, IET Control Theory Appl. 11 (6) (2017 Jan 9) 883–889.

[35] Z. Shao, Z. Xiang, Design of an iterative learning control law for a class of switched repetitive systems, Circuits Syst Signal Process. 36 (2) (2017 Feb 1) 845–866.

[36] Z. Shao, S. Huang, Z. Xiang, Robust ∞ repetitive control for a class of linear stochastic switched systems with time delay, Circuits Syst. Signal Process. 34 (4) (2015 Apr 1) 1363–1377.

[37] A. Reznik, M.G. Simoes, A. Al-Durra, S.M. Muyeen, *LCL* filter design and performance analysis for grid-interconnected systems, IEEE Trans. Ind. Appl. 50 (2) (2014 Mar) 1225–1232.

[38] J. Dannehl, M. Liserre, F.W. Fuchs, Filter-based active damping of voltage source converters with *LCL* filter, IEEE Trans. Ind. Electron. 58 (8) (2011 Aug) 3623–3633.